Pressure-induced structural and electronic phase transitions of uranium trioxide

Jiang-Jiang Ma,[1,2] Cheng-Bin Zhang,[1,2] Ruizhi Qiu,[3] Ping Zhang,[4,5] Bingyun Ao ⬤,[3,*] and Bao-Tian Wang ⬤[1,2,6,†]

[1]*Institute of High Energy Physics, Chinese Academy of Sciences (CAS), Beijing 100049, China*
[2]*Spallation Neutron Source Science Center, Dongguan 523803, China*
[3]*Science and Technology on Surface Physics and Chemistry Laboratory, Mianyang 621908, Sichuan, China*
[4]*School of Physics and Physical Engineering, Qufu Normal University, Qufu 273165, China*
[5]*Institute of Applied Physics and Computational Mathematics, Beijing 100088, China*
[6]*Collaborative Innovation Center of Extreme Optics, Shanxi University, Taiyuan, Shanxi 030006, China*

The crystal structures, phonon spectra, and electronic properties of uranium trioxide (UO_3) under high pressure have been systematically explored using a particle swarm optimization structure prediction method in conjunction with first-principles calculations. Our calculated lattice constants and the transition pressure of the two experimentally reported phases of γ- and η-UO_3 are consistent with previous experiments. At pressures of 13, 62, 220 GPa, three new structures of $P6_3/mmc$, $Pm\overline{3}n$, and $Fm\overline{3}m$ are predicted in sequence to be thermodynamically stable. Based on our calculated elastic constants and phonon spectra, we indicate that these three phases are mechanically and dynamically stable. Interestingly, upon phase transition from $P6_3/mmc$ to $Pm\overline{3}n$, UO_3 undergoes a semiconductor-to-metal electronic transition. In addition, we report results of specific heat, entropy, bulk modulus, shear modulus, Young's modulus, Poisson's ratio, and Debye temperature. Our results provide key insights into understanding the structural as well as the electronic behaviors of UO_3 under the condition of external pressure.

I. INTRODUCTION

Actinides have received much attention not only owing to their technological significance in nuclear energy applications, but also with respect to their intriguing physical properties due to the partially filled $5f$ electrons [1–3]. The $5f$ electrons have substantially large relativistic effects, itinerant or localized features, and multiple competing states. These complex electronic behaviors have led to fascinating structures, magnetic states, and also physical properties. Actinide oxides, as one of the most challenging systems in actinides, exhibit a broad range of oxidation states because of the hybridization among actinide-$5f6d$ and O-$2p$ orbitals [4,5]. Changing the chemical surrounding or external environment will greatly influence their structures and electronic states. In a nuclear fuel cycle, the actinide dioxides AnO_2 (An = Th, U, Np, Pu, Am, Cm, etc.) are the most stable and the most relevant members [2]. Many experimental and theoretical works have focused on AnO_2 [1,2,6–9]. In our previous studies [8,10–14] we also paid attention to AnO_2. We systematically investigated the ground-state properties (and high-pressure behaviors) of AnO_2, including ThO_2 [10], NpO_2 [11], PuO_2 [12], AmO_2 [14], UO_2 [13], and CmO_2 [8]. At ambient conditions, all of these AnO_2 crystallize in a high-symmetry cubic fluorite structure with space group $Fm\overline{3}m$. Under pressure, the $Fm\overline{3}m$ structure of UO_2 [13,15,16], ThO_2 [6,10,17], and PuO_2 [12,18,19] undergoes a transition to a low-symmetry

orthorhombic structure. Upon compression, especially after the structural phase transition, the electronic structure, magnetic state, phonon vibrations, elastic, and thermodynamic properties are greatly changed.

Compared with actinide dioxide, the higher oxides are coexistent with different oxidation states in nuclear fuels and have more complicated crystal structures. Moreover, it is difficult to prepare single crystals of such systems [4]. Up to now, there is a paucity of data in the literature for the higher actinide oxides. Uranium trioxide (UO_3), with the highest oxygen content in a solid U-O system, is a significant intermediate material in the nuclear fuel cycle [20,21]. UO_3 can be generated in the ore milling and refinement stages in the nuclear fuel cycle, in reprocessing of the spent nuclear fuel, or by heating uranyl nitrate in vacuum [4,22]. At ambient conditions there are six known different crystalline polymorphs of UO_3, including α-, β-, γ-, δ-, ε-, and ζ-UO_3 [23]. These structural forms have been well characterized using x-ray diffraction (XRD) or neutron diffraction techniques [24–31] and a portion of UO_3 pure phases including α, β, and γ phases have been measured by visible/near IR diffuse reflectance spectra and Raman spectra [32,33]. Under high pressure conditions, an earlier study [34] based on XRD has reported the seventh polymorphs (η-) at ∼3 GPa. Brincat *et al.* [35] verified the thermodynamic stability of η-UO_3 at high pressure using first-principles calculation. However, the pressure-induced structural transitions and electronic features of UO_3 are still poorly understood. A complete study in this respect is helpful for understanding its various structures and particular properties under the condition of hydrostatic compression.

---

*Corresponding author: aobingyun@caep.cn
†Corresponding author: wangbt@ihep.ac.cn

In our present work we extensively investigate the pressure-induced phase transitions of UO_3 and the corresponding structural, elastic, dynamic, and electronic properties up to 300 GPa using crystal structure prediction and first-principles calculations. Our calculations support the existence of the pressure-induced structural transition from the γ to η phase at $\sim$3 GPa [34,35]. By further gradually increasing pressure, we find three new stable crystalline structures: $P6_3/mmc$, $Pm\bar{3}n$, and $Fm\bar{3}m$. The symmetry of them is increased in sequence. We study in detail these new crystal structures together with their dynamical and mechanical stability, and corresponding thermodynamic properties, elastic properties, and electronic band structures, at their corresponding stable pressure ranges. Our findings indicate that the UO_3 displays a rich family of structural phases and appears as an insulator-to-metal electronic transition at high pressure.

We organize the paper as follows. In the following section we present our calculation methodology. In Sec. III we give the results and discussion of structural phase transitions, stability, and electronic structure. Finally, we conclude the main findings in Sec. IV.

II. COMPUTATIONAL DETAILS

To determine the stable structures of UO_3 at various pressures, we carried out a systematic structural search utilizing the particle swarm optimization (PSO) methodology as implemented in the CALYPSO code [36,37], which is not affected by any prior known structure and only depends on the knowledge of the chemical composition and external conditions. Such an approach has warranted its success in being used to predict various kinds of compounds, such as the high-temperature superconductors of hydrogen sulfide [38,39] and LaH_{10} [40,41]. Also, it has been used in the study of the high-pressure crystal structures of uranium dioxide [19] and hydride systems [42–45]. In the structure search of UO_3, the number of generations was set to be 30 and each generation contains 30 structures. It should be noted that the complex experimental structures, such as γ-$Fddd$ with 128 atoms and γ-$I4_1/amd$ with 64 atoms in their unit cells [29], have not been reproduced in the present study due to the limitation of the computational resource.

Subsequently, all candidate structures from our own searches combined with previously reported structures [29,34] were applied to structural optimization and total energy calculations, which were performed at the level of density functional theory (DFT) using the Vienna *ab initio* simulation package (VASP) [46]. The generalized gradient approximation (GGA) with the Perdew-Burke-Ernzerhof (PBE) functional was chosen for the exchange-correlation functional [47]. The electron-ion interaction was described by applying the projector augmented-wave method (PAW) [48]. In the electron configuration of UO_3, since the U-5f electrons have the greatest degree of direct participation in the chemical bonding, the f orbitals are nominally empty. Thus, the spin-polarization calculations are always converged to a nonmagnetic state [5,35] and our present calculations also support this fact. In our following study, all calculations were conducted with settings of spin unpolarized.

Besides, previous computational works on UO_3 [5,35,49] have proved that the DFT+U scheme improves the calculations in capturing the structures and band gaps over the standard DFT, and infer that +U is essential to simulate UO_3. This method strongly depends on the Hubbard effective parameter U-J, which can be labeled as one single parameter U for simplicity. The parameter in the DFT+U correction was originally derived by Dudarev *et al.* [50–52], based on the experimental measurements on UO_2. Work in the literature [53] has demonstrated that changing the effective U parameter mainly affects the predicted band gap. Since there is no parameter available for UO_3, we performed an assessment of the band gap dependence on U parameter, verifying that the U parameter in a range of 3–4 eV would be the most appropriate value for UO_3 polymorph (see the Appendix). For convenience of the calculation and comparison, the Hubbard terms were set as $U = 4.5$ eV and $J = 0.54$ eV, which also have been validated by Brincat *et al.* [35].

In our calculations, the spin-orbital coupling (SOC) has not been taken into account because it does not have significant effects on the results. In our previous work [13] we have carefully analyzed the inclusion of SOC on uranium dioxide. We found that the inclusion of SOC gives an improved descriptions of the magnetic state and ground-state electronic structures, but has very limited influence on macroscopic properties, such as pressure-induced phase transition, equation of states, phonon dispersions, and elastic properties. Since our current work focuses on structural transitions and stabilities of UO_3 under high pressure, the DFT+U formalism is good enough for those properties, and our results should be reliable even without SOC.

During each structural relaxation under corresponding pressure conditions, the convergence criteria of the total energy and forces were set as 1×10^{-6} eV and 0.01 eV/Å, respectively. An energy cutoff of 500 eV and appropriate Monkhorst-Pack [54] $\boldsymbol{k}$ meshes were chosen. For different phase structures, we refer to the general rule "$a \cdot k_a \approx b \cdot k_b \approx c \cdot k_c \approx 30$" ($a$, b, and c are lattice parameters in unit of Å), which has been used for our study of uranium oxide [5]. To examine the dynamic stability of our predicted phases, phonon calculations were performed by using a supercell approach as implemented in the PHONOPY package [55].

III. RESULTS AND DISCUSSIONS

A. Pressure-induced phase transitions

In order to search stable phases of UO_3 under pressure, a systematic structure prediction is performed at a series of pressure points (0, 20, 50, 100, 150, 200, 250, and 300 GPa). After accurate optimizing, we obtain a series of low-energy structures. The experimentally known α ($P\bar{3}m1$, $C2mm$, $C2$) [27,56], β ($P2_1$) [28], and δ ($Pm\bar{3}m$) [30] phases are successfully reproduced, validating the reliability of our methodology. The thermodynamic stability under pressure is evaluated by calculating the enthalpies for all UO_3 phases across the full pressure range of 0–300 GPa.

The enthalpy differences curves relative to the δ-UO_3 as a function of pressure are shown in Fig. 1. One can see that

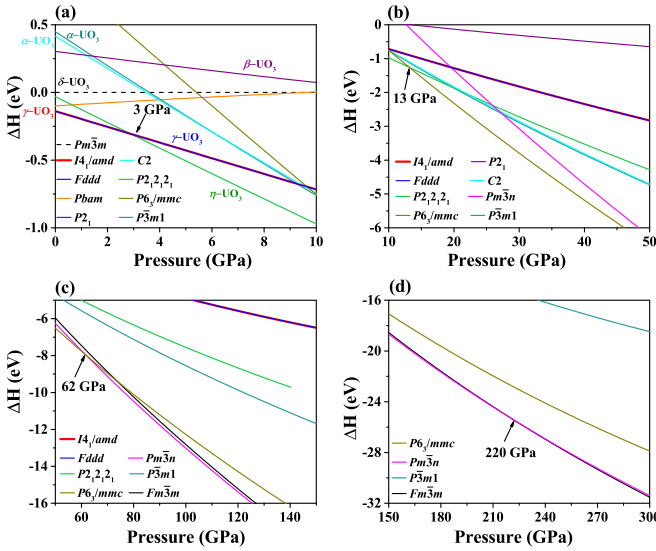FIG. 1. The relative enthalpy curves as a function of pressure for UO_3 from 0 to 300 GPa. The enthalpy of the $Pm\bar{3}m$ phase is set as zero for reference.

both the $Fddd$ and $I4_1/amd$ phases can be viewed as the ground state at ambient pressure, since their enthalpies are almost the same in a wide pressure range. In experiments, both $Fddd$ and $I4_1/amd$ phases are regarded as the γ-UO_3, which is the thermodynamically stable structure at oxygen pressures <10 atm [4]. Loopstra *et al.* [29] have performed neutron diffraction experiments on γ-UO_3 over a range of temperature, identifying it exists as three phases including

$I4_1/amd$ at 373 K, $Fddd$ at 293 K, and $Fddd$ at 77 K. The $Fddd$ phase is a maximal subgroup of $I4_1/amd$ and has twice the number of atoms of $I4_1/amd$. Although they belong to different space groups, our calculated as well as previously reported [29,35] enthalpies and energies per formula unit are essentially identical (see Fig. 1 and Table I). Thus, both $Fddd$ and $I4_1/amd$ phases could potentially be the ground state at ambient pressure. In the following, if not specially stated, γ-UO_3 would refer to the $I4_1/amd$ phase. Since we only focus on the pressure effects in our present work, not temperature, here we would not discuss in detail the temperature-induced phase transitions in UO_3.

Comparing with γ-UO_3 phase, the enthalpy differences at ambient pressure are 0.59, 0.55, 0.44 and 0.14 eV for $P\bar{3}m1$, $C2$, $P2_1$, and $Pm\bar{3}m$ phases, respectively, which are consistent with previously reported data [35]. Upon compression, the η ($P2_12_12_1$) phase gradually becomes stable and the γ-to-η phase-transition pressure is ~3 GPa, in good agreement with previous experimental and theoretical reports [34,35]. Further increasing the pressure, three energetically favorable high-pressure phases are predicted: $P6_3/mmc$, $Pm\bar{3}n$, and $Fm\bar{3}m$. The corresponding phase-transition pressures are 13, 62, and 220 GPa, respectively. Therefore, the sequence of high-pressure phase transitions of UO_3 is $Fddd$ or $I4_1/amd(\gamma) \rightarrow P2_12_12_1(\eta) \rightarrow P6_3/mmc \rightarrow Pm\bar{3}n \rightarrow Fm\bar{3}m$. This phase transition process shows that the pressure can induce an enhancement of the structural symmetry compared with the low-symmetry phases of γ and η. Even though the results are encouraging, three new phases from theoretical prediction still need to be verified in a future experiment.

TABLE I. Calculated lattice parameters, Wyckoff positions, and energy of various UO_3 phases at select pressures.

Space group	Pressure (GPa)	Lattice parameters (Å, deg)	Wyckoff positions	Energy (eV/f.u.)
$Fddd$	0	$a = 9.936$, $b = 20.667$, $c = 9.925$ $\alpha = \beta = \gamma = 90°$ $a = 9.823$, $b = 19.849$, $c = 9.632$ [29] $a = 9.94$, $b = 20.68$, $c = 9.93$ [35]	U1 16c 0.000 0.000 0.000 U2 16f 0.125 0.875 0.435 O1 32h 0.752 0.001 0.317 O2 32h 0.275 0.025 0.161 O3 32h 0.275 0.025 0.484	-34.86 -34.970 [35]
$I4_1/amd$	0	$a = b = 7.025$, $c = 20.654$ $\alpha = \beta = \gamma = 90°$ $a = b = 6.901$, $c = 19.975$ [29] $a = b = 7.020$, $c = 20.680$ [35]	U1 8c 0.000 0.000 0.000 U2 8e 0.000 0.250 0.565 O1 16h 0.000 0.049 0.089 O2 16h 0.000 0.003 0.433 O3 16h 0.000 0.551 0.234	-34.863 -34.970 [35]
$P2_12_12_1$	3	$a = 5.312$, $b = 5.522$, $c = 7.721$ $\alpha = \beta = \gamma = 90°$ $a = 5.220$, $b = 5.470$, $c = 7.510$ [34] $a = 5.340$, $b = 5.560$, $c = 7.760$ [35]	U 4a 0.783 0.389 0.174 O1 4a 0.412 0.873 0.579 O2 4a 0.418 0.6370.250 O3 4a 0.534 0.365 0.588	-34.730 -34.820 [35]
$P6_3/mmc$	50	$a = b = 3.868$, $c = 5.998$ $\alpha = \beta = 90°$, $\gamma = 120°$	U 2c 0.333 0.667 0.250 O1 2b 0.000 0.000 0.250 O2 4f 0.333 0.667 0.947	-32.921
$Pm\bar{3}n$	200	$a = b = c = 3.859$ $\alpha = \beta = \gamma = 90°$	U 2a 0.000 0.000 0.000 O 6c 0.250 0.000 0.500	-26.916
$Fm\bar{3}m$	250	$a = b = c = 4.775$ $\alpha = \beta = \gamma = 90°$	U 4a 0.000 0.000 0.000 O1 8c 0.250 0.250 0.250 O2 4b 0.500 0.500 0.500	-24.782

(a) γ-*Fddd* $U_{32}O_{96}$

γ-*I4$_1$/amd* $U_{16}O_{48}$

(b) *P2$_1$2$_1$2$_1$* U_4O_{12}

7-fold

(c) *P6$_3$/mmc* U_2O_6

11-fold

(d) *Pm$\overline{3}$n* U_2O_6

12-fold

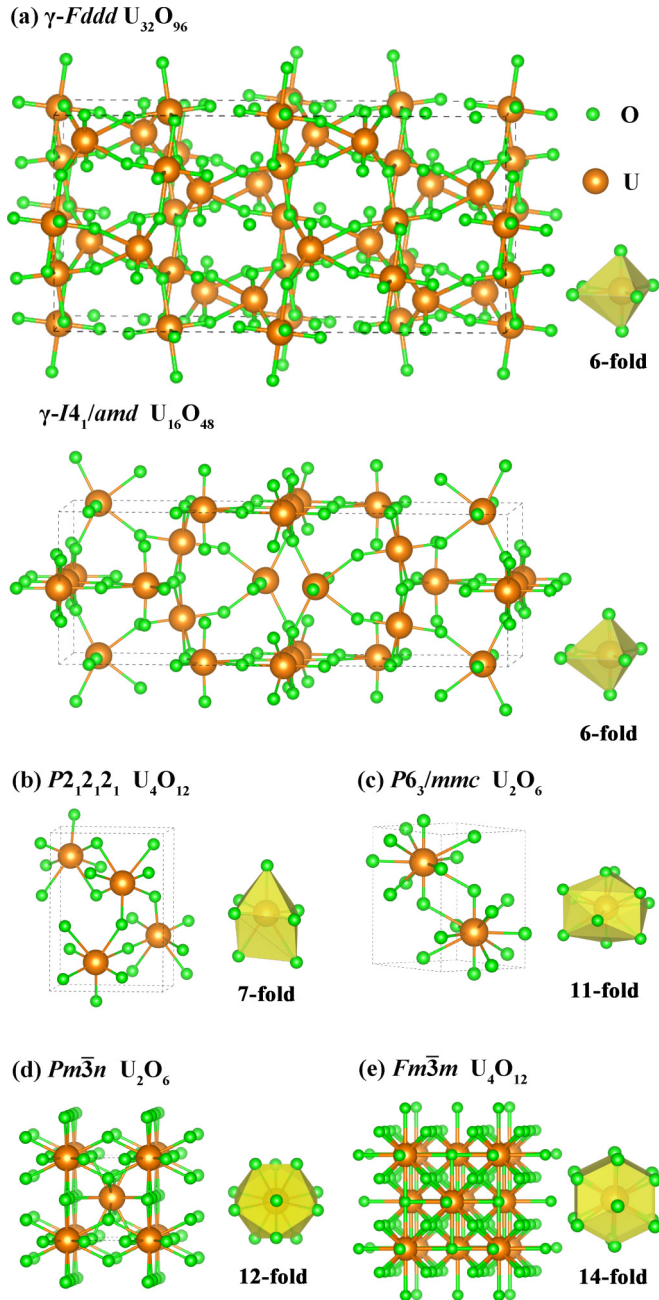**(e)** *Fm$\overline{3}$m* U_4O_{12}

14-fold

FIG. 2. Structural features of stable UO_3 phases at different pressures: (a) *Fddd*, *I4$_1$/amd* at 0 GPa, (b) *P2$_1$2$_1$2$_1$* at 3 GPa, (c) *P6$_3$/mmc* at 50 GPa, (d) *Pm$\overline{3}$n* at 200 GPa, and (e) *Fm$\overline{3}$m* at 250 GPa. In all these structures, green and orange spheres represent O and U atoms, respectively.

The lattice parameters, atomic coordinates, and total energies for the six phases at their energetically stable pressures are listed in Table I. For comparison, we also present the previous experimental and theoretical data [29,34,35]. As shown, our optimized lattice constants of the γ and η phases are in good agreement with those data. The structural features of *Fddd* ($U_{32}O_{96}$), *I4$_1$/amd* ($U_{16}O_{48}$), *P2$_1$2$_1$2$_1$* (U_4O_{12}), *P6$_3$/mmc* (U_2O_6), *Pm$\overline{3}$n* (U_2O_6), and *Fm$\overline{3}$m* (U_4O_{12}) are presented in Fig. 2. The *P6$_3$/mmc* structure belongs to the hexagonal lattice. Its primitive cell has two formula units (f.u.)

of UO_3. In this phase, the anions occupy two nonequivalent sites, while the U atoms are located in the long diagonal of the hexagonal lattice and are surrounded by 11 O atoms in a trigonal icosahedron. The *Pm$\overline{3}$n* phase crystallizes in the cubic system with two f.u. in the unit cell. In this phase, the arrangement pattern of U atoms forms a bcc sublattice, and there are 12 O atoms surrounding each U atom, forming an U-O icosahedron. Notably, the *Pm$\overline{3}$n* phase is isostructural to the proposed low-temperature phase of α-UH$_3$ [57–60]. The *Fm$\overline{3}$m* phase also crystallizes in a cubic system with four f.u. in its unit cell, which is isostructural with the fcc phase of PuH$_3$ [61]. In *Fm$\overline{3}$m* phase, the U atom is coordinated by 14 O atoms in a rhombic dodecahedron configuration, showing the highest coordination number. Comparing with the low-pressure *Fddd*, *I4$_1$/amd*, and *P2$_1$2$_1$2$_1$* phases, the U atoms in *Fm$\overline{3}$m* phase are hypercoordinated. Hence, the compression will increases the coordination number of the U atom. Such pressure-induced behavior has also been found in AcH$_2$ [62] and FeP$_2$ [63]. Additionally, the U sublattice of *Fm$\overline{3}$m* UO_3 is the same with that of *Fm$\overline{3}$m* UO_2, which belongs to the fluorite structure [13]. The main difference arises in the extra O anion sublattice at the 4*b* Wyckoff site. Similar cases have been identified in other high uranium oxides, such as U_2O_5 [53,64], U_3O_7 [65,66], and U_3O_8 [67,68]. These works show that it is possible to stabilize the fluoritelike of rich-O U-O compounds at high temperature and pressure. We note that the primitive cell of *Fm$\overline{3}$m* UO_3 has only one f.u. In our following calculations of its dynamical and electronic properties, the primitive cell is adopted.

B. Dynamical and mechanical stability

In addition to the enthalpy calculations, we also calculate the phonon and elastic properties to verify the dynamical and mechanical stability of our predicted phases.

The calculated phonon dispersions and partial phonon density of states (PhDOSs) of *P6$_3$/mmc*, *Pm$\overline{3}$n*, and *Fm$\overline{3}$m* phases at their energetically stable pressures of 50, 200, and 250 GPa, respectively, are displayed in Fig. 3. The primitive cell of *P6$_3$/mmc* and *Pm$\overline{3}$n* phases has eight atoms (double f.u. of UO_3), while the *Fm$\overline{3}$m* phase only has four atoms (one U and three O). So, there are 24 and 12 phonon modes for *P6$_3$/mmc* (*Pm$\overline{3}$n*) and *Fm$\overline{3}$m* phases, respectively. It is noteworthy that there are no negative phonon frequencies in the Brillouin zone. So, all our predicted structures of UO_3 are dynamically stable.

As shown, the highest vibrational frequencies of *Pm$\overline{3}$n* phase is larger than that of the *P6$_3$/mmc* phase, indicating that the pressure strengthens the interaction between cations and anions. Besides, the PhDOSs of the three phases can be viewed as two parts. The U atom mainly contributes to the low-frequency vibrations because of its relatively heavier mass, while the O atom dominates the high-frequency vibrations. The coupling between the optic and acoustic modes for *P6$_3$/mmc* and *Pm$\overline{3}$n* is evident, while such coupling for *Fm$\overline{3}$m* is negligible. The optic to acoustic mode ratio for *P6$_3$/mmc* and *Pm$\overline{3}$n* is larger than that of the *Fm$\overline{3}$m*. Thus, the lattice thermal conductivity for the two former phases may be lower than that for the third one. In our next work we may mainly focus on this point, but not here. Besides, comparing
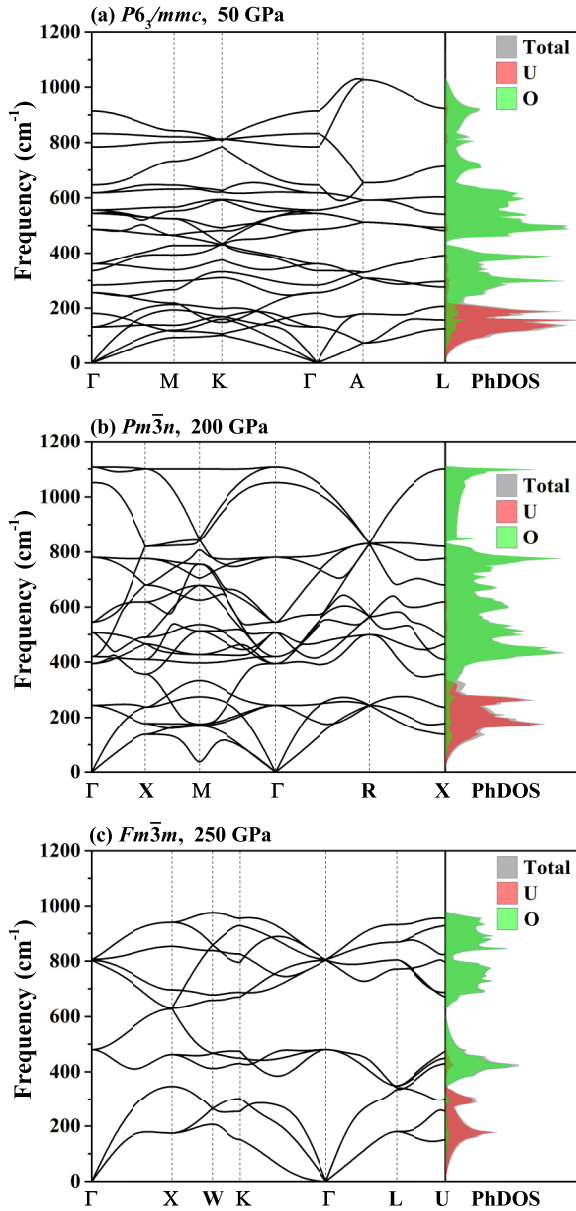
FIG. 3. Calculated phonon dispersions as well as PhDOSs for (a) $P6_3/mmc$ phase at 50 GPa, (b) $Pm\bar{3}n$ phase at 200 GPa, and (c) $Fm\bar{3}m$ phase at 250 GPa.
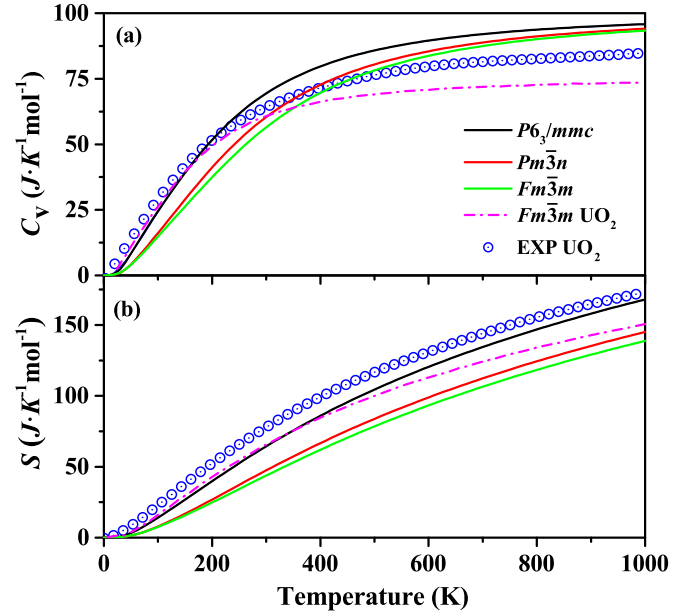

FIG. 4. Temperature dependencies of (a) specific heat at constant volume and (b) entropy for $P6_3/mmc$, $Pm\bar{3}n$, and $Fm\bar{3}m$ phases of UO_3 at 50, 200, and 250 GPa, respectively. Results of the $Fm\bar{3}m$ UO_2 from DFT [13] and experiments [70,71] are presented for comparison.

with the phonon modes of UO_2 [13], the lowest acoustic mode along the Γ-K of UO_3 shows evident soft behavior. This indicates a potential easy slipping direction along the [110].

Based on the total energy and PhDOS, we further calculate the thermodynamic properties including specific heat and entropy. The specific heat at constant volume C_V can be calculated by the derivative of the energy versus temperature [12]

$$C_V = \left(\frac{\partial E}{\partial T} \right)_V$$
$$= \sum_{qv} k_B \left(\frac{\hbar\omega(qv)}{k_B T} \right)^2 \frac{\exp\frac{\hbar\omega(qv)}{k_B T}}{\left[\exp\left(\frac{\hbar\omega}{k_B T} \right) - 1 \right]^2} \quad (1)$$

and the entropy S can be calculated by the derivative of the Helmholtz free energy versus temperature

$$S = -\frac{\partial F}{\partial T}$$
$$= \frac{1}{2T} \sum_{qv} \hbar\omega(qv)\coth\left(\frac{\hbar\omega(qv)}{2k_B T} \right)$$
$$- k_B \sum_{qv} \ln\left[2\sinh\left(\frac{\hbar\omega(qv)}{2k_B T} \right) \right], \quad (2)$$

where q is the wave vector, v is the index of phonon mode, ω is the phonon frequency, k_B is the Boltzmann constant, $\hbar$ is the reduced Planck constant, and T is the temperature.

Our calculated C_V and S are shown in Fig. 4. It can be seen that the C_V increases quickly up to room temperature and becomes close to a constant in the Dulong-Petit limit [69]. The temperature-dependent behaviors of the S are similar with that of UO_2 [13] at ambient condition. Over 50 K, the S of UO_3 becomes slightly large. Additionally, after phase transitions of $P6_3/mmc \rightarrow Pm\bar{3}n \rightarrow Fm\bar{3}m$, the values of C_V and S are reduced.

The elastic constants measure the response of crystal structure to external strain, and also impose constrains on the structural stability. Here the mechanical stability of UO_3 under high pressure is evaluated by calculating the elastic constants with the energy-strain method. Our calculated elastic constant, various moduli, Poisson's ratio, density, elastic wave velocities, and Debye temperatures for high-pressure phases of UO_3 are presented in Table II. Obviously the positive value of the elastic constant matrix of UO_3 at different pressures indicate that they are elastically stable. The mechanical stability criteria for the $P6_3/mmc$ structure are [72] $C44 > 0$,

TABLE II. Calculated elastic constants (GPa), bulk modulus B (GPa), shear modulus G (GPa), Young's modulus E (GPa), G/B ratio, Poisson's ratio (ν), density ρ (g/cm^3), transverse v_t (m/s), longitudinal v_l (m/s), average v_m (m/s) sound velocities, and Debye temperature Θ_D (K) for $P6_3/mmc$, $Pm\bar{3}n$, and $Fm\bar{3}m$ phases of UO$_3$ at 50, 200 and 250 GPa, respectively.

	$P6_3/mmc$	$Pm\bar{3}n$	$Fm\bar{3}m$
C_{11}	516.1	1115.3	1284.8
C_{12}	245.5	786.3	880.9
C_{13}	228.8	–	–
C_{33}	836.9	–	–
C_{44}	127.7	349.0	620.8
B	357.2	896.0	1015.5
G	150.3	258.1	369.3
E	395.5	706.4	1052.0
G/B	0.4	0.3	0.4
ν	0.315	0.369	0.327
ρ	12.2	16.5	17.5
v_t	3508.3	3845.1	4764.9
v_l	6757.1	8428.9	9405.1
v_m	3926.5	4334.1	5341.1
Θ_D	547.7	680.8	839.0

$C_{11} > |C_{12}|$, $(C_{11} + 2C_{12})C_{33} > 2C_{13}^2$, while for the $Pm\bar{3}n$ and $Fm\bar{3}m$ structures are $C_{11} > 0$, $C_{44} > 0$, $C_{11} > |C_{12}|$, $C_{11} + 2C_{12} > 0$.

We find that the elastic constants for our predicted three high-pressure phases of UO$_3$ satisfy the above conditions, confirming their mechanical stabilities. All the elastic constants for three phases in the considered pressure increase with increasing pressure. The elastic constant C_{11} is related to the axial compression along the principal crystallographic directions, and the C_{44} represents the deformation in shape [73]. For the three phases, it is obvious that C_{11} is almost two/three times of C_{44}, indicating that the high-pressure phases of UO$_3$ present a higher resistance to the axial compression than the shear deformation.

Based on our calculated elastic constants, the bulk modulus B and shear modulus G are calculated from the Voigt-Reuss-Hill (VRH) approximations [51,52,74] through $B = 1/2(B_v + B_R)$ and $G = 1/2(G_v + G_R)$. The Young's modulus E and Poisson's ratio ν are calculated through $E = 9BG/(3B + G)$ and $\nu = (3B - 2G)/[2(3B + G)]$. The Debye temperature Θ_D can be determined from the elastic constants within the Debye theory, in which the vibrations of solid are considered as elastic waves. The Debye temperature of the solid is related to an averaged sound velocity [75], which is calculated by

$$\Theta_D = \frac{h}{k_B}\left(\frac{3n}{4\pi\Omega}\right)^{1/3} v_m, \qquad (3)$$

where h and k_B are Planck and Boltzmann constants, respectively, n is the number of atoms in the molecule, Ω is molecular volume, and v_m is the average sound wave velocity. Approximately, v_m can be given by

$$v_m = \left[\frac{1}{3}\left(\frac{2}{v_t^3} + \frac{1}{v_l^3}\right)\right]^{-1/3}, \qquad (4)$$

where $v_t = \sqrt{G/\rho}$ (ρ is the density) is the transverse elastic wave velocity and $v_l = \sqrt{(3B + 4G)/3\rho}$ is the longitudinal elastic wave velocity.

As indicated in Table II, pressure-induced enhancements of the elastic constants, elastic moduli, elastic wave velocities, and Debye temperatures are evident. Only the Poisson's ratio is an exception. The shear modulus and Young's modulus of the $Fm\bar{3}m$ phase are very high compared to other two phases, indicating its great resistivity towards the compression. The values of the shear modulus and Young's modulus of the $P6_3/mmc$ UO$_3$ at 50 GPa are smaller than those of $Fm\bar{3}m$ UO$_2$ at 40 GPa [13]. This indicates that, comparing with UO$_2$, UO$_3$ is relatively easy to be compressed. Such a difference may originate from their different oxidation states. High oxidation states of uranium or plutonium may soften the oxides and lower their stability [4,5]. According to Pugh's criteria [76,77], the ratio of G/B determines the ductile or brittleness of material. If the value of $G/B < 0.57$, then materials show ductile behavior, otherwise is brittleness. Our calculated value indicates that the UO$_3$ in these phases show a ductile character. The Poisson's ratio ν provides the information about compressibility of materials. The calculated ν shows that the $P6_3/mmc$ phase is more compressible compared to $Pm\bar{3}n$ and $Fm\bar{3}m$ phases. The enhancements of the wave velocities and Debye temperature under pressure also supply useful information for high-pressure phases of UO$_3$.

C. Electronic structure

In general, structural transitions are always accompanied by the redistribution of electrons. To investigate the electronic properties of UO$_3$ under pressure, the electronic band structures of our predicted three phases at selected pressures are calculated and are shown in Fig. 5. It can be seen that the $P6_3/mmc$ UO$_3$ at 50 GPa shows semiconductor behavior with an indirect band gap of $\sim$2.07 eV between the Γ and M points. For $Pm\bar{3}n$ and $Fm\bar{3}m$ phases, there are no insulating band gaps. Both of these phases exhibit metallic characteristics, especially the $Pm\bar{3}n$. Similar with the $P6_3/mmc$, the valence band is mainly contributed by O-$2p$ while the conduction band is mainly U-$5f$. The difference is that several energy bands cross the Fermi energy in $Pm\bar{3}n$ phase. Both U-$5f$ and O-$2p$ states contribute to the valence and conduction bands around the Fermi level. This feature reveals the hybridization between U-$5f$ and O-$2p$ electrons. The $Fm\bar{3}m$ phase shows the characteristic of semimetal. As shown in Fig. 5(c), the partially occupied valence band top and conduction band bottom cross the Fermi level and locate at different high symmetry points of Γ and X, respectively. There is a continuous band gap, not an insulating band gap, between the mainly O-$2p$ occupied valence band and the mainly U-$5f$ occupied conduction band. Unlike the common metal, there are very few states at the Fermi energy level. So, the metallic nature of the $Fm\bar{3}m$ phase is weak. Obviously the electronic properties of UO$_3$ are sensitive to the applied pressure. According to our results, we find the semiconductor-to-metal-to-semimetal electronic transitions following the structural transitions of $P6_3/mmc \rightarrow Pm\bar{3}n \rightarrow Fm\bar{3}m$.

To obtain deeper insight into the electronic structures of UO$_3$ under pressure, we calculate the total electronic density
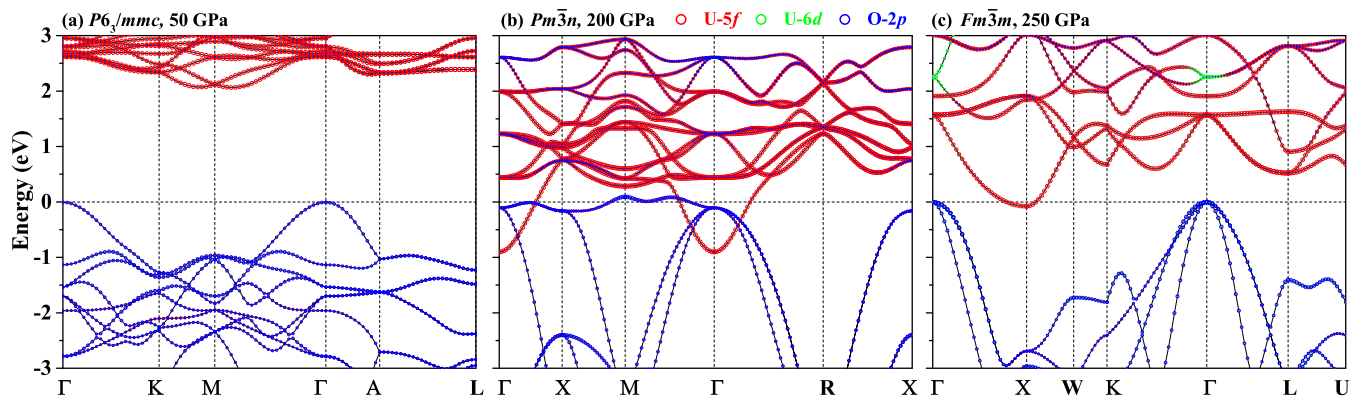
FIG. 5. Electronic band structures for (a) $P6_3/mmc$ phase at 50 GPa, (b) $Pm\bar{3}n$ phase at 200 GPa, and (c) $Fm\bar{3}m$ phase at 250 GPa. The size of the circles of the electronic band is proportional to the contribution of U-$5f$, U-$6d$, and O-$2p$ electrons.

of states (TDOSs) as well as the projected density of states (PDOSs) of U-$5f$ and O-$2p$ orbitals for all five phases, as shown in Fig. 6. It is clear that the band gap of UO_3 gradually decreases with elevated pressure and eventually closes, becoming a metal. Our calculated band gap for the ground state γ-UO_3 is ~2.88 eV, in good agreement with previous works [5]. As mentioned in the literature [5,35,49], the band
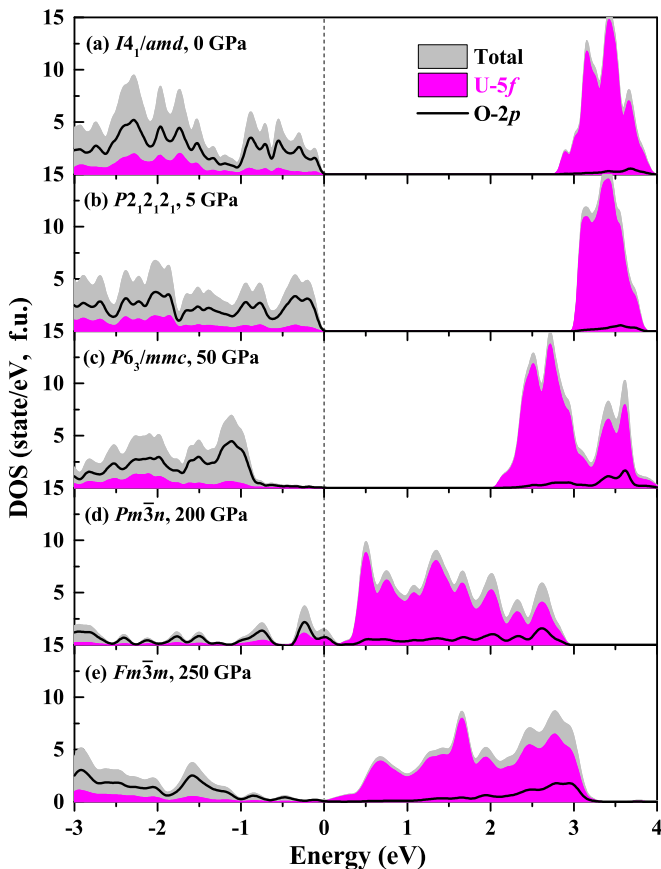

FIG. 6. TDOSs and PDOSs for (a) $I4_1/amd$ phase at 0 GPa, (b) $P2_12_12_1$ phase at 5 GPa, (c) $P6_3/mmc$ phase at 50 GPa, (d) $Pm\bar{3}n$ phase at 200 GPa, and (e) $Fm\bar{3}m$ phase at 250 GPa. The Fermi energy level is set as zero and is denoted by the vertical dotted line.

gaps of all UO_3 polymorphs at ambient conditions are in the range of 0.64–3.21 eV. Although the band gaps of γ-, η-, and $P6_3/mmc$ UO_3 are comparable to those of $Fm\bar{3}m$ and $Pnma$ phases of UO_2 [13], the electronic structures are very different. For UO_2, which is a Mott insulator, both the top of the valence band and the bottom of the conduction band mainly consist of U-$5f$ orbitals, which lead to the localized behaviors of the $5f$ electrons. In contrast to UO_2, the valence band of UO_3 is mainly associated with the O-$2p$ orbitals with a small partial of the U-$5f$ orbitals. The conduction band is mainly from the U-$5f$ orbitals, with less presence of the O-$2p$ orbitals. According to previous reports [35] as well as our present work, the α-, β-, γ-, δ-, and η-UO_3 as well as $P6_3/mmc$ UO_3 are described as charge-transfer insulators and the U-$5f$ electrons are manifested as exhibiting itinerant features. As mentioned in a recent study [78], comparing with UO_2, the higher oxides of U_3O_7 also exhibit a similar electronic structure, which may arise from the changes of coordination polyhedra and shorter U-O bonds.

Below the Fermi energy level, the O-$2p$ orbitals mainly contribute while the U-$5f$ orbitals partially contribute in the energy range of -3 to -2 eV. Comparing the TDOSs and PDOSs under different pressures, we find that the contributions of U-$5f$ orbitals on valence bands are gradually decreased with increasing pressure and upon the structural transitions. The compression will compel the U-$5f$ electrons to participate in the chemical bonding, realizing the increase of the coordination number for the high-pressure phases. For $Pm\bar{3}n$ phase there is a significant overlap between U-$5f$ and O-$2p$ electrons around the Fermi level, implying the strong coupling and covalent bonding between U and O atoms. In particular, the metallic state is kept in its stable pressure range. The $5f$ electrons in $Pm\bar{3}n$ and $Fm\bar{3}m$ exhibit evident itinerant behaviors.

To reveal the electron transfer behaviors of UO_3 under pressure, we calculate the line charge density along the U-O bonds and perform the Bader charge analysis [79]. The calculated partial charges and atomic volume for atom U and O are listed in Table III. In $P6_3/mmc$ and $Fm\bar{3}m$ phases, each U atom loses 3.02 and 2.95 electrons, respectively, which distribute unevenly surrounding the O atoms. In $Pm\bar{3}n$ phase, the U atom loses 2.88 electrons to neighboring O atoms.

TABLE III. Calculated partial charges and atomic volume for U and O in $P6_3/mmc$, $Pm\overline{3}n$, and $Fm\overline{3}m$ phases of UO$_3$ under pressures of 50, 200, and 250 GPa, respectively. The atom types and number in primitive cell are also listed.

Phase	Atom	No.	Partial charge (eV/atom)	Volume (Å^3/atom)
$P6_3/mmc$	U	2	+3.02	12.23
	O1	2	−1.12	9.96
	O2	1	−0.95	8.34
	O3	3	−0.95	8.36
$Pm\overline{3}n$	U	2	+2.88	10.39
	O	6	−0.96	6.12
$Fm\overline{3}m$	U	1	+2.95	9.91
	O1	1	−1.09	6.39
	O2	2	−0.93	5.46

These charges are evenly distributed among the neighboring O atoms. In addition, we find that the pressure-induced transition is always accompanied by a volume collapse of the U atom.

Using the AIM-UC software [80], we perform the bond critical point (BCP) search in order to discuss the bonding features. The characteristics at BCP, including Laplacian, curvature ratio, and ellipticity, are related to bonding features. For instance, the properties of the specified interaction between atoms can be expressed by a Laplacian and curvature ratio at BCP. The positive values of the Laplacian and the relatively small curvature ratio indicate closed-shell interactions, i.e., ionic bonding, otherwise, it is the shared interactions, i.e., covalent bonding [81]. The intermediate value between those exhibited by predominantly ionic and covalent bonds are pictured as being intermediate in character. In Table IV we present the calculated Hessian eigenvalues, Laplacian, curvature ratio, and ellipticity of the charge at BCP for U-O bonds in $P6_3/mmc$, $Pm\overline{3}n$, and $Fm\overline{3}m$ phases of UO$_3$ under pressure of 50, 200, and 250 GPa, respectively. At the same time, the bond lengths and line charge density at the corresponding bond points (CD$_b$) are also listed. In these phases, all of the Laplacian and curvature ratio are positive values, which indicated that the U-O bonds in UO$_3$ under high pressure are dominated by an ionic characteristic. However, the U-O2 bond in $P6_3/mmc$ possesses the lowest Laplacian value and the highest curvature ratio, which is similar to the U-O bond in δ-UO$_3$ [81]. This is most likely to be one of uranyl-like bonds with the covalentlike characteristic.

Moreover, the value of CD$_b$ can reflect to some extent the covalent or ionic features of a chemical bond [8,12]. Since the CD$_b$ value for U-O2 of 0.271 e/a.u.^{3} is greatly higher than 0.104 e/a.u.^{3} found for Si covalent bond [82], the U-O2 bonds in $P6_3/mmc$ phase show evident features of covalent and are much stronger than other U-O bonds. Our previous value for Si is under the condition of ambient pressure. Such a large CD$_b$ value of U-O2 is mainly due to its short bond length and under the condition of high pressure. Besides, the CD$_b$ value for U-O1 of 1.02 e/a.u.^{3} is also close to 0.104 e/a.u.^{3} for Si. Therefore, the U-O bonds in $P6_3/mmc$ exhibit a covalent characteristic. In $Pm\overline{3}n$ phase, the CD$_b$ value for its three U-O bonds of 0.123 e/a.u.^{3} is also larger than that of Si, indicating a covalent bonding feature. In $Fm\overline{3}m$ phase, the CD$_b$ of its U-O1 bonds is smaller than that of the U-O2 in $P6_3/mmc$ phase, while the covalent nature of its U-O1 is stronger than that of the U-O1 in $P6_3/mmc$ phase. Thus, the bond formation of three new phases is dominated by an ionic bond, also with less presence of covalent bonds, such as U-O1 and U-O2 in $P6_3/mmc$, U-O in $Pm\overline{3}n$, and U-O1 in $Fm\overline{3}m$. These characteristics are mainly originated from their different bond lengths. Shorter bond lengths would result in stronger covalent bonding.

IV. CONCLUSION

In summary, we systematically performed theoretical studies on the structural variability and associated physical properties of UO$_3$ under high pressure. Through a structure searching method and first-principles calculations, we have predicted three high-pressure phases, apart from the known ambient- or low-pressure phases. Our calculations suggest that the γ-UO$_3$ will first transform to η-UO$_3$ of $P2_12_12_1$ phase, agreeing with previous experiment studies, and then gradually change to the $P6_3/mmc$, $Pm\overline{3}n$, and $Fm\overline{3}m$ phases at pressures of 13, 62 and 220 GPa, respectively. The stabilities have been analyzed and warranted through calculating both phonon spectra and elastic constants. Based on our calculated phonon spectra and elastic constants, we further obtained the specific heat, entropy, various moduli, Poisson's ratio, elastic wave velocities, and Debye temperatures. The electronic structures show that there are electronic phase transitions along with the structural transitions: from the semiconducting state of low-pressure $P6_3/mmc$ phase to high-pressure metal and semimetal states of $Pm\overline{3}n$ and $Fm\overline{3}m$.

TABLE IV. BCP characteristics, bond length, and charge density at bond points (CD$_b$) for U-O bonds in $P6_3/mmc$, $Pm\overline{3}n$, and $Fm\overline{3}m$ phases of UO$_3$ under pressure of 50, 200, and 250 GPa, respectively.

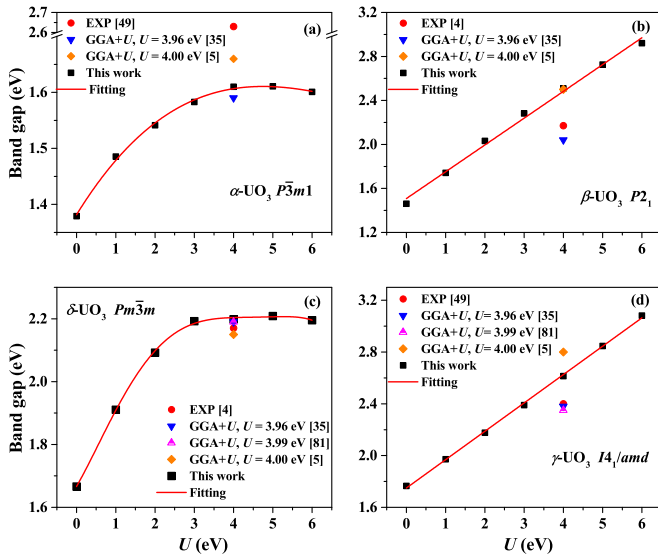| Phase	Bond	Hessian eigenvalues			Laplacian	Curvature ratio	Ellipticity	Bond length (Å)	CD$_b$ (e/a.u.^{3})
		λ_1	λ_2	λ_3					
$P6_3/mmc$	U-O1	−3.602	−2.805	12.305	+5.898	+0.293	0.284	2.234	0.102
	U-O2	−12.350	−11.868	22.330	+1.887	+0.553	0.041	1.819	0.271
	U-O3	−1.364	−1.251	6.676	+4.061	+0.204	0.090	2.527	0.049
$Pm\overline{3}n$	U-O	−4.485	−4.135	15.761	+7.142	+0.285	0.085	2.157	0.123
$Fm\overline{3}m$	U-O1	−5.881	−5.877	18.179	+6.421	+0.324	0.001	2.067	0.151
	U-O2	−2.190	−2.190	9.558	+5.178	+0.229	0	2.387	0.075

FIG. 7. The band gaps of (a) α-, (b) β-, (c) δ-, and (d) γ-UO$_3$ calculated by the GGA+U formalism with U in the range of 0–6 eV. For comparison, experimental [4,49] and other theoretical [5,35,81] results are also presented.

Upon compression, the coordinate number, elastic constants, elastic moduli, elastic wave velocities, and Debye temperatures are gradually increased while the band gap is decreased to zero. The symmetry of the phases is also enhanced to high-symmetry cubic structures. The find of the $Fm\overline{3}m$ phase has indicated that the UO$_3$ may be synthesized by UO$_2$ under conditions of high pressure, high temperature, and abundant oxygen. Our studies enrich the phase diagram of UO$_3$ under pressure and would be helpful for further understanding structural and physical properties of the whole U-O solid system.

APPENDIX

The DFT+U method has achieved a wide array of successes in resolving strongly correlated and localized $5f$ electronic systems, such as UO$_2$. Unfortunately, there are no parameters available for UO$_3$ so far. To verify the applicability of the Hubbard parameter for the UO$_3$ polymorph in this work, we perform a complete DFT+U calculation, wherein we vary the U from 0 to 6 eV. In order to compare the experiment values directly, we calculate the band gaps of $P\overline{3}m1$ (α-), $P2_1$ (β-), $Pm\overline{3}m$ (δ-), and $I4_1/amd$ (γ-) UO$_3$ using the experimental lattice constants [28–30,56]. In Fig. 7 we present the band gaps dependence on the Hubbard parameter U for UO$_3$, by comparing with available experimental [4,49] and theoretical [5,35,81] values. It is clear, from these findings at least, that the U value has an important influence on the band gap. The calculated band gap for UO$_3$ increases with increasing U. Especially for β- and γ-UO$_3$, their band gaps increase linearly with increasing U. By comparing with the experimental [4,49] and theoretical [5,35,81] values, we find that the U values in the range of 3–4 eV are the most reasonable values. For the α- and δ-UO$_3$, their band gaps no longer increase after U increased to 4 and 3 eV, respectively, at which the values of their band gaps are close to the experimental results [4,49]. Overall, comparing with the experimental [4,49] and theoretical [5,35,81] results, the accuracy of the band gap for these UO$_3$ phases is satisfactory by tuning the U parameter in a range of 3–4 eV with GGA+U approach.

Moreover, in order to assess the dependence of electronic structure on Hubbard parameter U for three new structures of $P6_3/mmc$, $Pm\overline{3}n$, and $Fm\overline{3}m$ under pressure, we plot in Fig. 8 the total DOS and PDOS with $U = 0$, 3, and 6 eV. One can see that the band gap of $P6_3/mmc$ increases with the increasing of U. The trend is similar with our finding for β- and γ-UO$_3$. However, the electronic structure of $Pm\overline{3}n$ and $Fm\overline{3}m$ metal
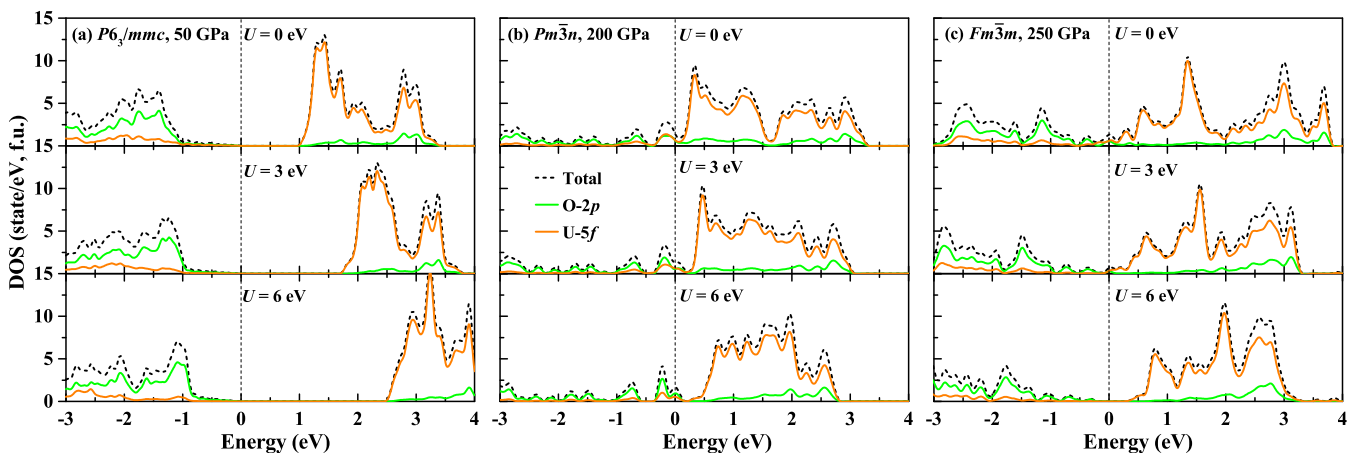

FIG. 8. The total DOS for the (a) $P6_3/mmc$, (b) $Pm\overline{3}n$, and (c) $Fm\overline{3}m$ phase calculated within GGA+U formalism with $U = 0$, 3, and 6 eV. The projected DOSs for the U-$5f$ and O-$2p$ orbitals are also shown. The Fermi energy level is set at zero.

phases is less affected by increasing U, which only suppresses a tiny contribution of U-$5f$ around the Fermi level for $Fm\bar{3}m$ phase. As for the $Pm\bar{3}n$ phase, both the O-$2p$ and the U-$5f$ states cross the Fermi energy and have a minor contribution around the Fermi level, which reveal the small hybridization between U-$5f$ and O-$2p$ electrons. These features are not changed with the different U values, constantly keeping its weak metal behavior.

[1] I. D. Prodan, G. E. Scuseria, and R. L. Martin, Phys. Rev. B **76**, 033101 (2007).

[2] L. Petit, A. Svane, Z. Szotek, W. M. Temmerman, and G. M. Stocks, Phys. Rev. B **81**, 045108 (2010).

[3] K. T. Moore and G. van der Laan, Rev. Mod. Phys. **81**, 235 (2009).

[4] H. Idriss, Surf. Sci. Rep. **65**, 67 (2010).

[5] B. Ao, R. Qiu, J. Tang, and J. Chen, J. Nucl. Mater. **543**, 152563 (2021).

[6] M. Idiri, T. Le Bihan, S. Heathman, and J. Rebizant, Phys. Rev. B **70**, 014113 (2004).

[7] P. Santini, S. Carretta, G. Amoretti, R. Caciuffo, N. Magnani, and G. H. Lander, Rev. Mod. Phys. **81**, 807 (2009).

[8] L. Hou, W.-D. Li, F. Wang, O. Eriksson, and B.-T. Wang, Phys. Rev. B **96**, 235137 (2017).

[9] J.-B. Morée, R. Outerovitch, and B. Amadon, Phys. Rev. B **103**, 045113 (2021).

[10] B.-T. Wang, H. Shi, W.-D. Li, and P. Zhang, J. Nucl. Mater. **399**, 181 (2010).

[11] B.-T. Wang, H. Shi, W. Li, and P. Zhang, Phys. Rev. B **81**, 045119 (2010).

[12] P. Zhang, B.-T. Wang, and X.-G. Zhao, Phys. Rev. B **82**, 144110 (2010).

[13] B.-T. Wang, P. Zhang, R. Lizárraga, I. Di Marco, and O. Eriksson, Phys. Rev. B **88**, 104107 (2013).

[14] Y. Lu, Y. Yang, F. Zheng, B.-T. Wang, and P. Zhang, J. Nucl. Mater. **441**, 411 (2013).

[15] U. Benedict, G. Andreetti, J. Fournier, and A. Waintal, J. Phys. (France) Lett. **43**, 171 (1982).

[16] P. C. M. Fossati, L. Van Brutzel, A. Chartier, and J.-P. Crocombette, Phys. Rev. B **88**, 214112 (2013).

[17] J.-P. Dancausse, E. Gering, S. Heathman, and U. Benedict, High Press. Res. **2**, 381 (1990).

[18] H. X. Song, H. Y. Geng, and Q. Wu, Phys. Rev. B **85**, 064110 (2012).

[19] H. X. Song, L. Liu, H. Y. Geng, and Q. Wu, Phys. Rev. B **87**, 184103 (2013).

[20] I. J. Schwerdt, C. G. Hawkins, B. Taylor, A. Brenkmann, S. Martinson, and L. W. McDonald IV, Radiochim. Acta **107**, 193 (2019).

[21] M. P. Wilkerson, S. C. Hernandez, W. T. Mullen, A. T. Nelson, A. L. Pugmire, B. L. Scott, E. S. Sooby, A. L. Tamasi, G. L. Wagner, and J. R. Walensky, Dalton Trans. **49**, 10452 (2020).

[22] L. E. Sweet, T. A. Blake, C. H. Henager, S. Hu, T. J. Johnson, D. E. Meier, S. M. Peper, and J. M. Schwantes, J. Radioanal. Nucl. Chem. **296**, 105 (2013).

[23] H. R. Hoekstra, S. Siegel, and F. X. Gallagher, J. Inorg. Nucl. Chem. **32**, 3237 (1970).

[24] H. Hoekstra and S. Siegel, J. Inorg. Nucl. Chem. **18**, 154 (1961).

[25] R. d. Engmann and P. De Wolff, Acta Cryst. **16**, 993 (1963).

[26] V. Wheeler, R. Dell, and E. Wait, J. Inorg. Nucl. Chem. **26**, 1829 (1964).

[27] B. O. Loopstra and E. H. P. Cordfunke, Recl. Trav. Chim. Pays-Bas **85**, 135 (1966).

[28] P. Debets, Acta Cryst. **21**, 589 (1966).

[29] B. Loopstra, J. Taylor, and A. Waugh, J. Solid State Chem. **20**, 9 (1977).

[30] M. Weller, P. Dickens, and D. Penny, Polyhedron **7**, 243 (1988).

[31] E. Enriquez, G. Wang, Y. Sharma, I. Sarpkaya, Q. Wang, D. Chen, N. Winner, X. Guo, J. Dunwoody, J. White *et al.*, ACS Appl. Mater. Interfaces **12**, 35232 (2020).

[32] L. E. Sweet, D. D. Reilly, D. G. Abrecht, E. C. Buck, D. E. Meier, Y.-F. Su, C. S. Brauer, J. M. Schwantes, R. G. Tonkyn, T. A. Szecsody, J. E. Blake, and T. J. Johnson, in *Optics and Photonics for Counterterrorism, Crime Fighting and Defence IX; and Optical Materials and Biomaterials in Security and Defence Systems Technology X* (International Society for Optics and Photonics, Bellingham, WA, 2013), Vol. 8901, p. 890107.

[33] T. L. Spano, A. E. Shields, B. S. Barth, J. D. Gruidl, J. L. Niedziela, R. J. Kapsimalis, and A. Miskowiec, Inorg. Chem. **59**, 11481 (2020).

[34] S. Siegel, H. Hoekstra, and E. Sherry, Acta Cryst. **20**, 292 (1966).

[35] N. A. Brincat, S. C. Parker, M. Molinari, G. C. Allen, and M. T. Storr, Inorg. Chem. **53**, 12253 (2014).

[36] Y. C. Wang, J. Lv, L. Zhu, and Y. M. Ma, Comput. Phys. Commun. **183**, 2063 (2012).

[37] Y. Wang, J. Lv, L. Zhu, and Y. Ma, Phys. Rev. B **82**, 094116 (2010).

[38] Y. Li, J. Hao, H. Liu, Y. Li, and Y. Ma, J. Chem. Phys. **140**, 174712 (2014).

[39] A. Drozdov, M. Eremets, I. Troyan, V. Ksenofontov, and S. I. Shylin, Nature (London) **525**, 73 (2015).

[40] H. Liu, I. I. Naumov, R. Hoffmann, N. Ashcroft, and R. J. Hemley, Proc. Natl. Acad. Sci. USA **114**, 6990 (2017).

[41] A. Drozdov, P. Kong, V. Minkov, S. Besedin, M. Kuzovnikov, S. Mozaffari, L. Balicas, F. Balakirev, D. Graf, V. Prakapenka *et al.*, Nature (London) **569**, 528 (2019).

[42] X. Wang, M. Li, F. Zheng, and P. Zhang, Phys. Lett. A **382**, 2959 (2018).

[43] I. A. Kruglov, A. G. Kvashnin, A. F. Goncharov, A. R. Oganov, S. S. Lobanov, N. Holtgrewe, S. Jiang, V. B. Prakapenka, E. Greenberg, and A. V. Yanilkin, Sci. Adv. **4**, eaat9776 (2018).

[44] D. Wang, H. Zhang, H.-L. Chen, J. Wu, Q.-J. Zang, and W.-C. Lu, Phys. Lett. A **383**, 774 (2019).

[45] X.-H. Wang, F.-W. Zheng, Z.-W. Gu, F.-L. Tan, J.-H. Zhao, C.-L. Liu, C.-W. Sun, J. Liu, and P. Zhang, ACS omega **6**, 3946 (2021).

[46] G. Kresse and J. Furthmüller, Phys. Rev. B **54**, 11169 (1996).

[47] J. P. Perdew and Y. Wang, Phys. Rev. B **45**, 13244 (1992).

[48] P. E. Blöchl, Phys. Rev. B **50**, 17953 (1994).

[49] H. He, D. A. Andersson, D. D. Allred, and K. D. Rector, J. Phys. Chem. C **117**, 16540 (2013).

[50] S. L. Dudarev, G. A. Botton, S. Y. Savrasov, C. J. Humphreys, and A. P. Sutton, Phys. Rev. B **57**, 1505 (1998).

[51] S. Dudarev, M. Castell, G. Botton, S. Savrasov, C. Muggelberg, G. Briggs, A. Sutton, and D. Goddard, Micron **31**, 363 (2000).

[52] S. Dudarev, D. N. Manh, and A. Sutton, Philos. Mag. B **75**, 613 (1997).

[53] M. Molinari, N. A. Brincat, G. C. Allen, and S. C. Parker, Inorg. Chem. **56**, 4468 (2017).

[54] H. J. Monkhorst and J. D. Pack, Phys. Rev. B **13**, 5188 (1976).

[55] A. Togo and I. Tanaka, Scr. Mater. **108**, 1 (2015).

[56] W. Zachariasen, Acta Cryst. **1**, 265 (1948).

[57] Y. Zhang, B. Wang, Y. Lu, Y. Yang, and P. Zhang, J. Nucl. Mater. **430**, 137 (2012).

[58] R. Mulford, F. Ellinger, and W. Zachariasen, J. Am. Chem. Soc. **76**, 297 (1954).

[59] H. Y. Lu, in *Materials Science Forum* (Trans Tech Publications, Switzerland, 2015), Vol. 817, pp. 675–684.

[60] C. D. Taylor, T. Lookman, and R. S. Lillard, Acta Mater. **58**, 1045 (2010).

[61] J.-J. Zheng, B.-T. Wang, I. Di Marco, and W.-D. Li, Int. J. Hydrog. Energy **39**, 13255 (2014).

[62] H. Jiang, W. Wang, C. Zhang, X.-N. Hu, G.-H. Zhong, X.-Q. Lu, and Y.-H. Su, Int. J. Hydrog. Energy **39**, 15827 (2014).

[63] K. Hu, J. Lian, L. Zhu, Q. Chen, and S.-Y. Xie, Phys. Rev. B **101**, 134109 (2020).

[64] D. Andersson, G. Baldinozzi, L. Desgranges, D. Conradson, and S. Conradson, Inorg. Chem. **52**, 2769 (2013).

[65] L. Desgranges, G. Baldinozzi, G. Rousseau, J.-C. Niepce, and G. Calvarin, Inorg. Chem. **48**, 7585 (2009).

[66] F. Garrido, R. Ibberson, L. Nowicki, and B. Willis, J. Nucl. Mater. **322**, 87 (2003).

[67] F. Zhang, M. Lang, J. Wang, W. Li, K. Sun, V. Prakapenka, and R. C. Ewing, J. Solid State Chem. **213**, 110 (2014).

[68] S. R. Spurgeon, M. Sassi, C. Ophus, J. E. Stubbs, E. S. Ilton, and E. C. Buck, Proc. Natl. Acad. Sci. USA **116**, 17181 (2019).

[69] C. Kittel, P. McEuen, and P. McEuen, *Introduction to Solid State Physics* (Wiley, New York, 1996), Vol. 8.

[70] F. Grønvold, N. J. Kveseth, A. Sveen, and J. Tichý, J. Chem. Thermodyn. **2**, 665 (1970).

[71] J. J. Huntzicker and E. F. Westrum, Jr., J. Chem. Thermodyn. **3**, 61 (1971).

[72] J. F. Nye *et al.*, *Physical Properties of Crystals: Their Representation by Tensors and Matrices* (Oxford University Press, Oxford, 1985).

[73] T. Yang, X. Zhu, J. Ji, and J. Wang, Sci. Rep. **10**, 1 (2020).

[74] R. Hill, Proc. Phys. Soc. London Sect. A **65**, 349 (1952).

[75] C. Cozzo, D. Staicu, J. Somers, A. Fernandez, and R. Konings, J. Nucl. Mater. **416**, 135 (2011).

[76] S. Pugh, Philos. Mag. **45**, 823 (1954).

[77] H. L. Kagdada, P. K. Jha, P. Śpiewak, and K. J. Kurzydłowski, Phys. Rev. B **97**, 134105 (2018).

[78] G. Leinders, G. Baldinozzi, C. Ritter, R. Saniz, I. Arts, D. Lamoen, and M. Verwerft, Inorg. Chem. **60**, 10550 (2021).

[79] W. Tang, E. Sanville, and G. Henkelman, J. Phys.: Condens. Matter **21**, 084204 (2009).

[80] D. Vega and D. Almeida, J. Comput. Methods Sci. Eng. **14**, 131 (2014).

[81] L. Casillas-Trujillo, G. Baldinozzi, M. K. Patel, H. Xu, and K. E. Sickafus, Phys. Rev. Mater. **1**, 065404 (2017).

[82] B.-T. Wang, P. Zhang, H.-L. Shi, B. Sun, and W.-D. Li, Eur. Phys. J. B **74**, 303 (2010).